Geomechanics and Engineering, *Vol. 28, No. 1* (*2022*) *25-33*
https://doi.org/10.12989/gae.2022.28.1.025

Dynamic response of free-end rod with consideration of wave frequency

Sang Yeob Kim[1], Jong-Sub Lee[2], Erol Tutumluer[1] and Yong-Hoon Byun*[3]

[1]*Department of Civil and Environmental Engineering, University of Illinois at Urbana-Champaign, 205 North Mathews Avenue, Urbana, IL 61801, USA*
[2]*School of Civil, Environmental and Architectural Engineering, Korea University, 145, Anam-ro, Seongbuk-gu, Seoul, 02841, South Korea*
[3]*School of Agricultural Civil & Bio-Industrial Engineering, Kyungpook National University, 80 Daehak-ro, Buk-gu, Daegu, 41566, South Korea*

(*Received July 22, 2021, Revised October 10, 2021, Accepted November 23, 2021*)

Abstract. The energy transferred on drill rods by dynamic impact mainly determines the penetration depth for in-situ tests. In this study, the dynamic response and transferred energy of drill rods are determined from the frequency of the stress waves. AW-type drill rods of lengths 1 to 3 m are prepared, and strain gauges and an accelerometer are installed at the head and tip of the connected rods. The drill rods are hung on strings, allowing free vibration, and then impacted by a pendulum hammer with fixed potential energy. Increasing the rod length L increases the wave roundtrip time ($2L/c$, where c is the wave velocity), and hence the transferred energy at the rod head. At the rod tip, the first velocity peak is higher than the first force peak because a large and tensile stress wave is reflected, and the transferred energy converges to zero. The resonant frequency increases with rod length in the waveforms measured by the strain gauges, and fluctuates in the waveforms measured by the accelerometer. In addition, the dynamic response and transferred energy are perturbed when the cutoff frequency is lower than 2 kHz. This study implies that the resonant frequency should be considered for the interpretation of transferred energy on drill rods.

Keywords: drill rod; dynamic response; free vibration; resonant frequency; transferred energy

1. Introduction

In the design and construction of on-ground geo-infrastructures, the engineering indices and properties of in-situ sediments are determined through geotechnical investigations. The standard penetration test (SPT) is a conventional in-situ test, which is available in most soil types using the dropping-hammer system (ASTM D1586, Hong *et al*. 2016). The SPT typically drives the rod into the ground under dynamic impacts by the hammer. The impact energy through an extended drill rod is sufficient to penetrate a specific deep layer (Bajaj and Anbazhagan 2019). Meanwhile, the dynamic cone penetration test (DCPT) using the dropping hammer system has been extensively used by researchers and practitioners since its first deployment in Australia in the mid 1950's (Scala 1956). The DCPT characterizes subsurface and road pavement in transportation engineering (Kleyn 1975, Webster *et al.* 1992, Gabr *et al*. 2000, Mohammadi *et al*. 2008, Kodicherla and Nandyala 2016). On shallow subsurface or weakly cemented layers, the dynamic cone penetrometer (DCP) is preferred because it imparts lower impact energy than the SPT (Langton 1999, Du *et al.* 2016, Mir *et al.* 2017, Lee and Byun 2020). Furthermore, the DCP can be extensively operated for deep soils when a weak layer is continuous throughout the depth profile.

Dynamic penetration tests such as SPT and DCPT impart a fixed impact energy, which can be expressed as the potential energy, depending on the falling height and weight of the hammer (ASTM D1586, ASTM D6951). Factors that influence energy loss are responsible for the difference between the potential and transferred energies (ASTM D4633, Kovacs 1979, Skempton 1986). During hammer dropping, energy is preliminarily lost to interferences of the free fall, such as friction between the hammer and guide and energy dissipation during the hammer–anvil contact (Lee *et al.* 2010). More recently, factors affecting the energy transferred through the drill rod to the cone tip have been identified (Byun and Lee 2013, Kim *et al.* 2019, Lee *et al.* 2019, Kim and Lee 2020). After the impact, additional energy is lost to friction between the drill rod and soils; moreover, the transferred energy depends on the strength characteristics of the target layer (Byun *et al.* 2014, Sujatha *et al*. 2018).

As the length of the drill rods increases during ground profiling, the energy transferred by the impacting drop hammer changes along the depth of the target layer. Several studies have suggested rod length factors for correcting the transferred energy (Seed *et al.* 1985, Skempton 1986, Morgano and Liang 1992, Youd and Idriss 2001). Although rod-lengthening enhances the energy loss, particularly in soft soils, long rods are heavier than shorter rods and impart more potential energy. A long drill rod with sufficient weight may compensate the energy loss (Daniel *et al*. 2005, Odebrecht *et al*. 2005, Sancio and Bray 2005). The effect of the rod length also depends on the strength characteristics of soils. For this reason, the intrinsic responses of the rod, such as the frequency response, must be interpreted from the waveforms measured by strain gauges and an accelerometer. Howie *et al*. (2003) demonstrated that an inappropriate level of low-pass filtering causes

*Corresponding author, Professor
E-mail: yhbyun@knu.ac.kr

ISSN: 2005-307X (Print), 2092-6219 (Online)

underestimates of the transferred energy, which are significant if the predominant frequency (i.e., the resonant frequency) is filtered. However, the effect of wave frequency on the dynamic responses of drill rods under free-end boundary conditions has not been investigated.

This study explores the dynamic response and transferred energy of a drill rod hung on strings, allowing consideration of the wave frequency under free-end conditions. It first discusses the specifications and experimental setup of the instrumented rod and the different rod-length cases. Next, the resonant frequencies in the different cases are extracted from the force and velocity waveforms. Finally, the effect of cutoff frequency on the transferred energy is discussed.

2. Materials and methods

2.1 Instrumented rod

In typical dynamic penetration tests, an anvil is directly impacted by a hammer. The impact energy is transferred through the drill rod to the tip of the penetrometer, which contacts the target layer. The present study employed AW-type drill rods with a diameter of 44.5 mm, which are generally used in SPTs. The rods were hung on strings to allow free vibration, eliminating soil friction effects. The transferred energies were estimated by strain gauges and an accelerometer installed in a 0.45-m length-instrumented rod [Fig. 1(a)]. Four strain gauges, each with a resistance of 350 Ω, were configured as a Wheatstone full-bridge circuit and were symmetrically attached to the drill rod to compensate the temperature effect and minimize eccentricity [Fig. 1(b)] (Byun and Lee 2013, Hong *et al*. 2016, Kim and Lee 2020).

The output voltage measured by the Wheatstone full-bridge circuit can be converted into a force by mechanical calibration, as shown in Fig. 2. A piezoelectric accelerometer (PCB Piezotronics, 350B01) used in this study had a maximum amplitude of 100,000 *g* and an upper-frequency limit of 10 kHz. Under the frequencies lower than the upper limit, the stable frequency response can be obtained from the accelerometer, whereas the measured vibration above the upper-frequency limit can deviate from the desired acceleration level with high measurement uncertainty. The accelerometer was mounted on the same section as the attached strain gauges. The accelerometer consisted of a piezoelectric crystal, a pre-load ring, a seismic mass, and housing Fig. 1(c). Under acceleration, the realignment and accumulation of the positively and negatively charged ions on the piezoelectric crystal are proportional to the force amplitude. The accelerometer components are designed to generate an electrical signal under a force-induced acceleration. By this mechanism, the accelerometer converts the motion, vibration, and shock signals to an electrical output signal. Thereafter, the acceleration amplitude can be estimated by calibrating the measured electrical signals against known acceleration values. In addition, the velocity can be calculated by integrating the measured acceleration and multiplying the result by the impedance of the drill rod to obtain a force unit as follows

$$F_{ac} = Z \cdot V_{ac} = \frac{E \cdot A}{c} \cdot V_{ac} \quad (1)$$

where F_{ac} is the force estimated by the accelerometer, and Z and V_{ac} are the impedance of the rod and the particle velocity calculated by integrating the acceleration, respectively. The variables E, A, and c are the elastic modulus, cross-sectional area, and wave velocity through the rod, respectively. Typical force waveforms estimated by the accelerometer and strain gauges at the head and tip of the rods located in borehole are presented in Fig. 3. Note that the lag between the waveforms at the head and tip of rods equals the rod length (L) divided by the wave velocity through the rods (c). Using the particle velocity estimated from the accelerometer (V_{ac}) and the force measured by the strain gauges (F_{sg}), the transferred energy (E) was determined by the force–velocity integration method (F–V method) as follows (ASTM D4633)

$$E = \int F_{sg} \times V_{ac}\, dt \quad (2)$$

In fact, the transferred energy can also be determined using the force squared integration method (F^2 method). However, the F^2 method requires several assumptions, such as determining the uniform cross-sectional area for the entire rod system (Sy and Campanella 1993). Considering the nonuniform rod-coupler system used in this study, the energies transferred through rods of various lengths were estimated using Eq. (2).

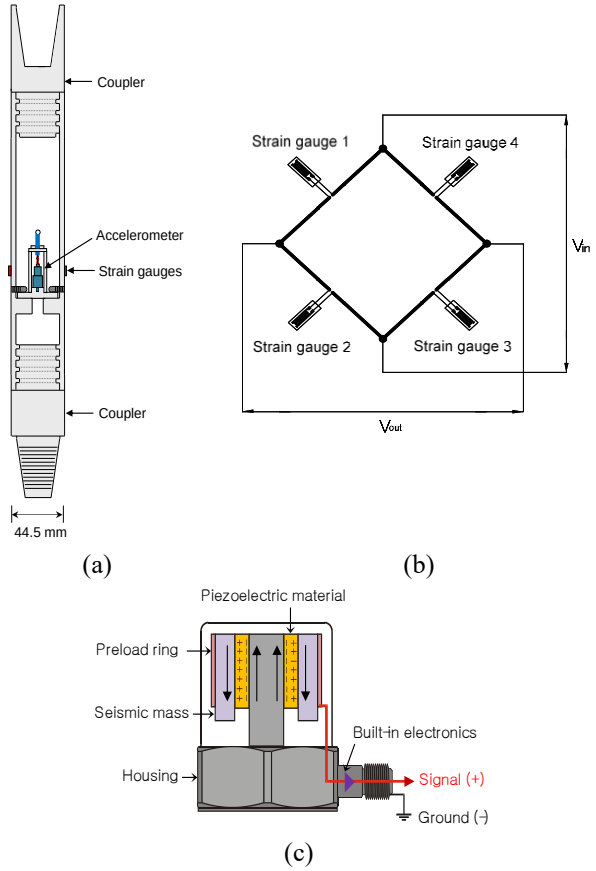

Fig. 1 Schematic drawing of (a) instrumented rod, (b) strain gauges, and (c) accelerometer

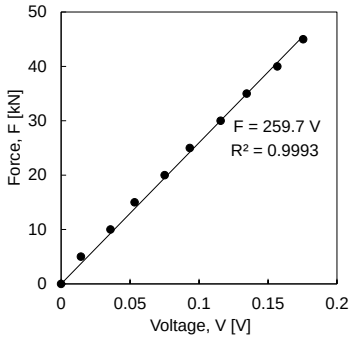

Fig. 2 Relationship between applied force and output voltage obtained from strain gauges

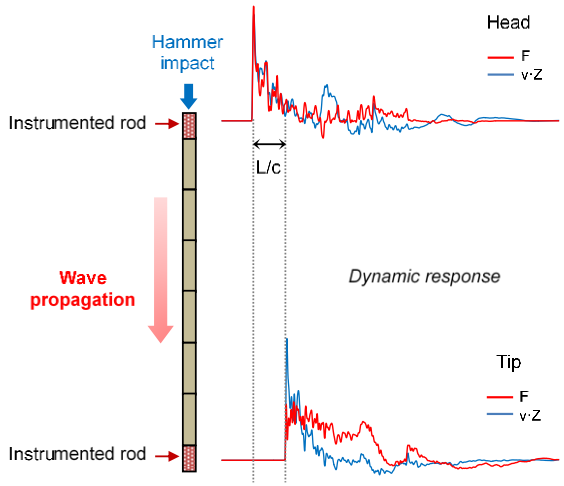

Fig. 3 Typical dynamic responses obtained from the instrumented drill rods in borehole

2.2 Test procedure

The dynamic responses of several drill rods hung by strings were investigated in this study. AW-type drill rods of 1-m length and fixed outside diameter (44.5 mm) were impacted by a 52-N weight pendulum hammer falling from a 30-cm height. The total lengths of the drill rods are summarized in Table 1. From the wave velocity in the steel rod, the roundtrip time was calculated as *2L/c* in all cases. When the drill rods were impacted by the pendulum hammer, the forces measured by the strain gauges and the acceleration captured by the accelerometer were acquired in a data logger. At the sampling rate of the data logger (96 kHz per channel), a maximum of 960 data points could be collected in 10 milliseconds (ms).

3. Results and discussion

3.1 Waveforms at rod head

The output signals at each impact on the drill rods were measured by strain gauges and an accelerometer as described above. Fig. 4 shows the force and velocity waveforms and the transferred energy detected at the head of the instrumented rods. Initially, the force and velocity increased in proportion, but were quickly desynchronized by wave reflections at the interface of the rod with a large cross-sectional area. The time *2L/c* in the force and velocity waveforms increased with increasing total length of the drill rod.

Table 1 Total length of drill rods and *2L/c* for three different rod lengths

Case	1m	2m	3m
Total length [m]	1.45	2.45	3.45
2L/c [ms]	0.57	0.96	1.35

When the dropped hammer contacted the rod head, the transferred energy rapidly increased to its maximum during the travel time (Fig. 4). As the first-cycle compressional wave was reflected at the tip and arrived at time *2L/c*, the maximum energy existed in the duration of *2L/c* after the first rise time in all three cases. Overall, the maximum energy at the rod head increased with rod length because the positive amplitudes of force and velocity increased with rod length. After the maximum energy, the transferred energy decreased slightly and then dropped significantly. Through subsequent wave cycles, the transferred energy fluctuated and finally converged to a constant value. Although all rods received the same constant input energy, the maximum energy depended on the rod length.

3.2 Waveforms at rod tip

Fig. 5 presents the force–velocity waveforms and the transferred energy detected at the tips of the instrumented rods. In all cases, the first velocity peak exceeded that imparted by the force. Different from the situation at the rod head, the force after the first peak decreased while the velocity increased. Under idealized free-end conditions, the force and velocity at the tip should be zero and twofold, respectively, because the stress wave reflected at the tip is typically large and tensile. However, in real rod systems, the sensors are difficult to place at the exact ending point. In addition, impedance changes cause initial reflections at the couplers located between the rods. Like the dynamic response of the rod head, the duration of *L/c* at the rod tip increased with rod length. Notably, the *2L/c* time at the head is equal to the *L/c* time at the tip due to the lag between the waveforms at the head and tip of rods. Increasing the rod length increased the interval between the compressional waves in the first and second cycles.

The transferred energy was lower at the tip than at the head because energy was lost during the wave propagation, as reported in previous studies (Abou-matar and Goble 2004, Byun and Lee 2013). The transferred energy waveforms also differed between the tip and the head. Overall, the transferred energy waveforms at the tip resembled a haversine pulse. The energy transferred at the tip increased to its maximum within *L/c* ms and then decreased rapidly to zero. The energy partially recovered as the cyclic compressional wave was transferred to the tip, but its amplitude decreased in successive cycles. The maximum energies were higher in the 2- and 3-m length

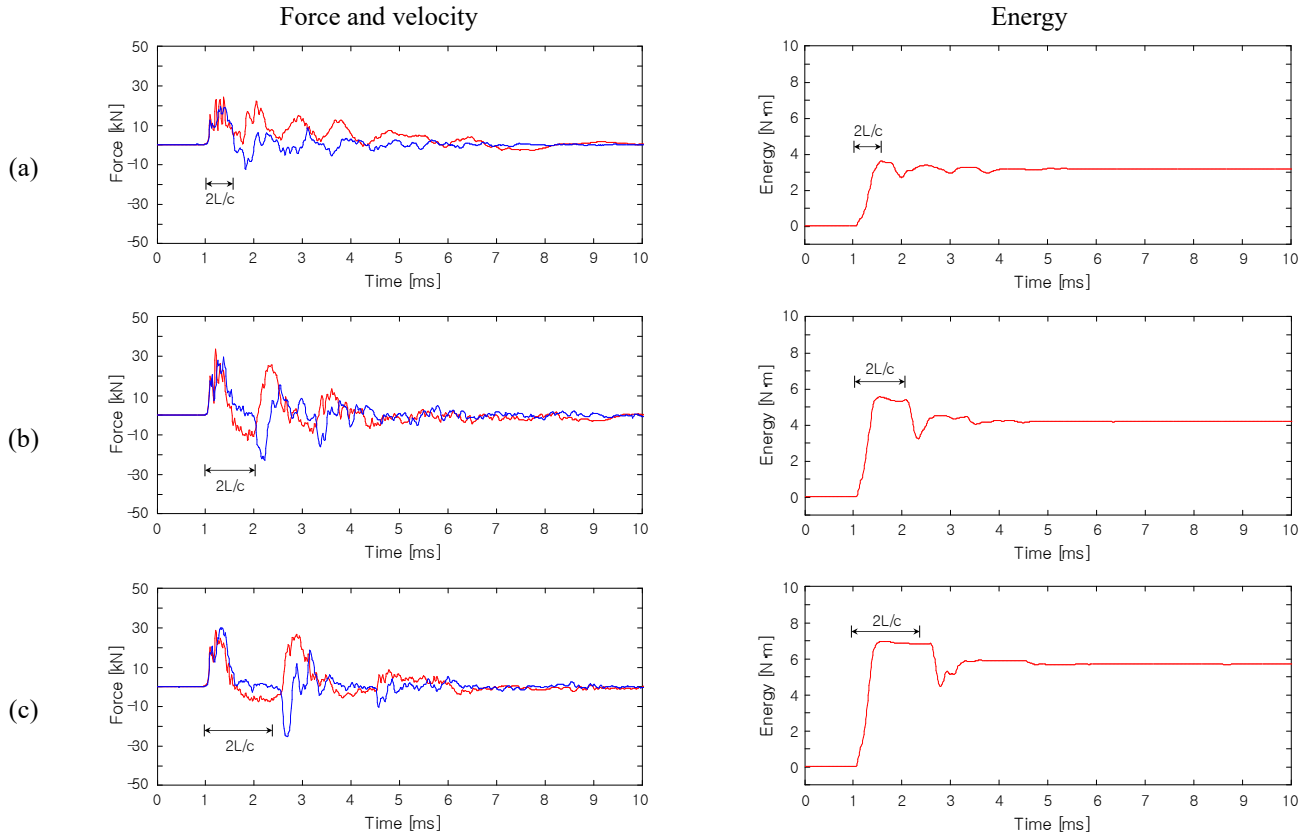

Fig. 4 Force–velocity waveforms and transferred energy waveforms detected at the head of rods with the lengths of (a) 1 m, (b) 2 m, and (c) 3 m. Blue and red lines indicate the force and velocity signals, respectively

rods than in the 1-m length rod because the 1st cycle stress wave traveling through the tip was not completely propagated in *L/c* time. In all cases, the energy at the tip eventually decayed to zero.

3.3 Resonant frequency

The resonant frequency is the highest-amplitude frequency in the frequency spectrum. To determine the resonant frequencies of force and velocity, the frequency spectra of the force–velocity waveforms were determined at the rod head and are graphed in Fig. 6. Large amplitudes were observed up to approximately 20 kHz in the accelerometer spectrum, and up to approximately 4 kHz in the strain-gauge spectra. In general, the dominant frequencies were lower in the strain gauge than in the accelerometer spectra. Fig. 7 shows the resonant frequencies at the tip and the head as functions of rod length. Figs. 7(a) and 6(b) present the results of the strain gauges and accelerometer, respectively (note that their *y*-axes have different scales). The resonant frequencies obtained from the strain gauges decreased with increasing rod length (from 1.2 to 0.44 kHz), and were similar at the head and tip. In contrast, the resonant frequencies from the accelerometer ranged between 0.51 and 10.0 kHz as the rod length increased. At both head and tip, the resonant frequencies from the accelerometer and strain gauges were close only for the longest rod. Thus, the resonant frequencies of the drill rods obtained from the accelerometer were less reliable than those obtained from the strain gauges.

For a finitely long rod with free ends, the natural frequency (f_n) is calculated as

$$f_n = \frac{\omega_n}{2\pi} = \frac{nv_c}{2l} \tag{3}$$

where ω_n and v_c are the circular frequency of a natural mode vibration and the wave-propagation velocity, respectively. The variables l and n denote the rod length and number of natural mode vibrations, respectively. In an undamped system, the natural frequency usually equals the resonant frequency. Fig. 8 compares the resonant frequencies of the first natural mode estimated by Eq. (3) and the resonant frequencies measured from the strain gauges. The resonant frequencies measured from the strain gauges were slightly smaller than the estimated values, showing the linear relationship with a coefficient of determination of 0.92. Thus, the dynamic responses of the drill rods can be more effectively characterized from strain-gauge data than from accelerometer data.

3.4 Effect of low-pass filtering

To investigate the effect of low-pass filtering on the dynamic response, nine low-pass filters with different cutoff frequencies (0.5–20 kHz) were applied. Fig. 9 shows the windowing functions of the nine lowpass filters. The

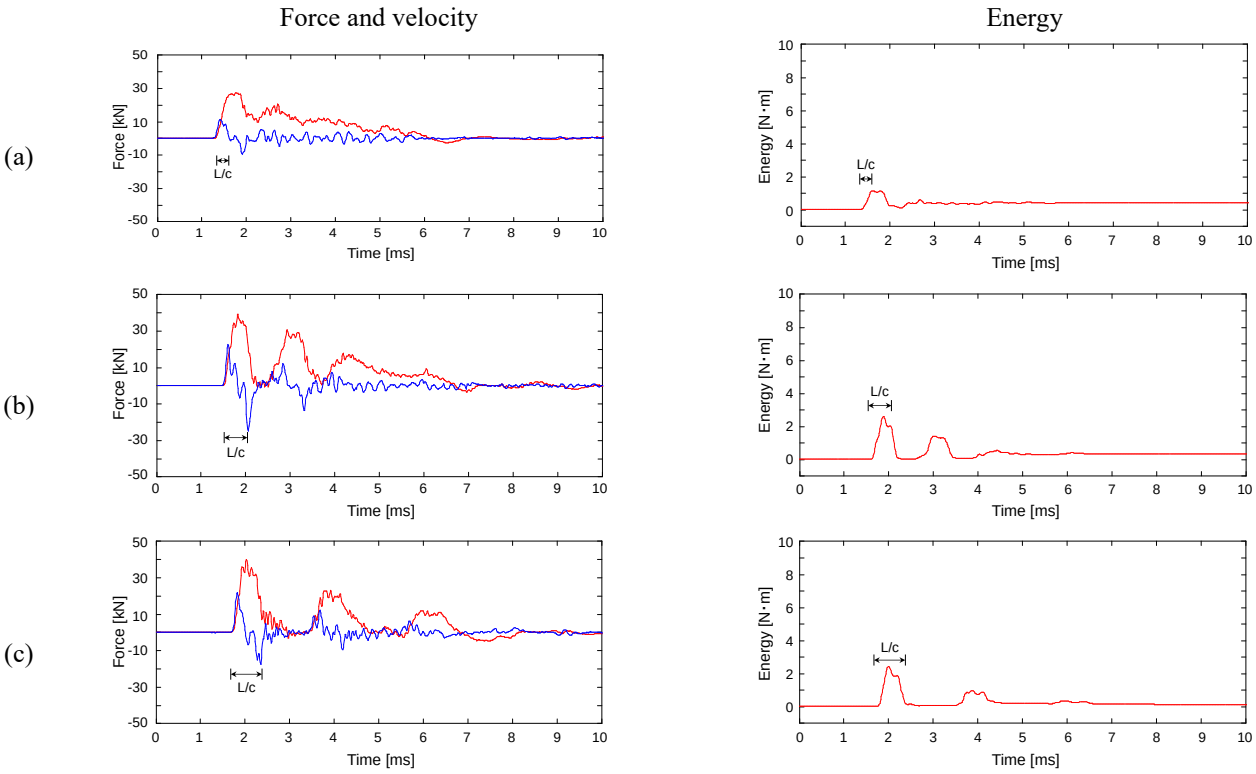

Fig. 5 Force–velocity waveforms and transferred energy waveforms detected at the tip of rods with the lengths of (a) 1 m, (b) 2 m, and (c) 3 m. Blue and red lines indicate the force and velocity signals, respectively.

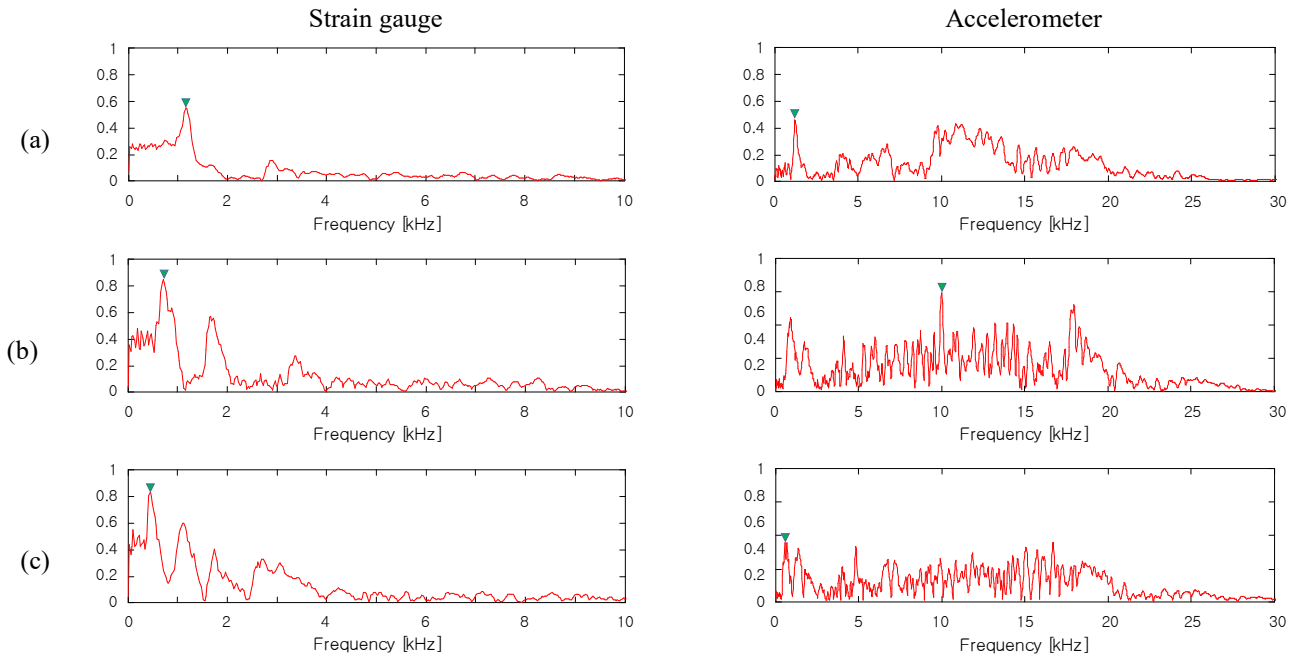

Fig. 6 Frequency responses of force and velocity at the rod head with the lengths of (a) 1 m, (b) 2 m, and (c) 3 m. Triangle symbol denotes the maximum amplitude in the frequency response at each signal

transition region between the passband and stopband of each filter was designed using the Hanning window function, and the transition width was constant. Note that Hanning windows facilitate rapid sidelobe decay. The force and velocity waveforms were applied to the filters, and then the transferred energy was reanalyzed by the F–V method. Although the acceleration measurements are often unreliable, the transferred energy in the F–V method can be evaluated through the complete waveform, which is restricted to the duration of the first compressional wave in the F^2 method. Fig. 10 shows typical waveforms at the head of the 2-m-long rod at different cutoff frequencies. When

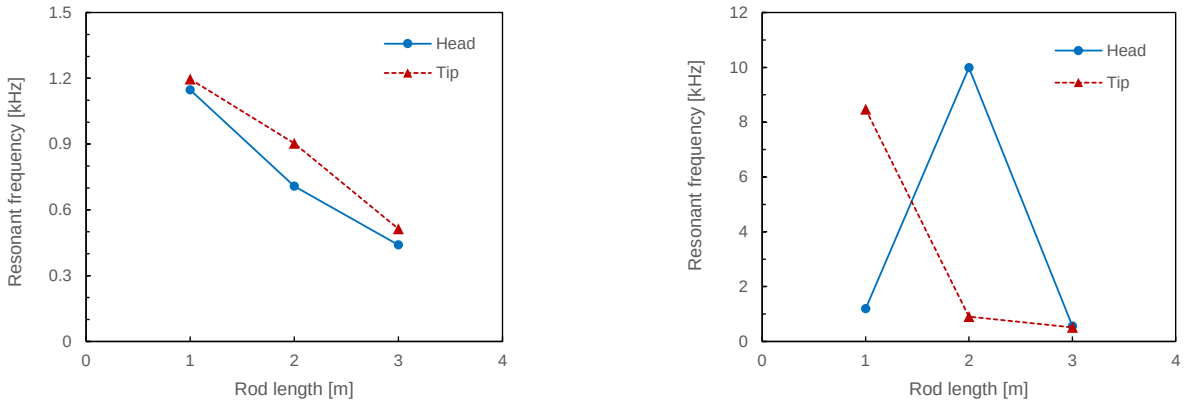

Fig. 7 Variation of resonant frequencies along the rod length obtained from (a) strain gauges and (b) accelerometer

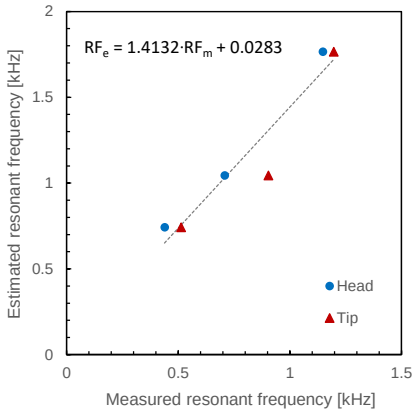

Fig. 8 Estimated resonant frequencies versus resonant frequencies measured from strain gauges. RF_e and RF_m denote the estimated and measured resonant frequencies, respectively

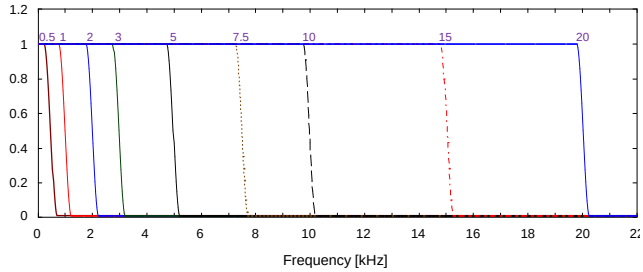

Fig. 9 Window functions for low-pass filtering with different cutoff frequencies. The number above each window function denotes the value of cutoff frequency

the cutoff frequency was 20 kHz, the force and velocity waveforms were almost identical to those of the original signal [Fig. 4(b)]. As the cutoff frequency decreased, the magnitude and first rising time of the waveforms gradually changed. At cutoff frequencies lower than 2 kHz, the magnitudes of the force and velocity waveforms significantly decreased, and the perturbation before the first rising time disturbed the exact determination of this time. Subsequently, the energy waveforms varied with cutoff frequency. At lower cutoff frequencies the maximum energy was lower than in the original signal.

The time *2L/c* is commonly used for estimating the transferred energy in dynamic penetration testing (Odebrecht *et al.* 2005, Lee and Byun 2020). The transferred energy at *2L/c* after low-pass filtering is plotted with respect to cutoff frequency in Fig. 11. The transferred energy at *2L/c* was almost independent of cutoff frequencies above 2 kHz. Below 2 kHz, the cutoff frequency affected the transferred energy at *2L/c* regardless of rod length and instrumented location. Especially at the tip of the 3-m-long rod, the transferred energy at 2L/c increased at the cutoff frequency of 1 kHz due to the signal distortion of force–velocity waveforms and the extension of the period for simultaneously positive force and velocity within 2L/c. Such signal distortion of force–velocity waveforms could also be found in Figure 10(d) compared with Fig. 10(c). Fig. 12 shows the transferred energy versus rod length at each cutoff frequency. The transferred energy at *2L/c* decreased with cutoff frequency below 2 kHz, except at the tip of the 3-m-long rod. Considering the range of resonant frequencies of the different rod lengths, the cutoff frequency should be higher than the resonant frequency. With a higher cutoff frequency, the transferred energy at the rod head at *2L/c* increased with increasing rod length [Fig. 12(a)] because the first stress wave in the shorter rods was reflected during *2L/c* before the wave propagation was completed. At the tip [Fig. 12(b)], the transferred energy was higher for the 2-m-long rods than for the 1-m-long rod. Especially at the tip of the 3-m-long rod, the transferred energy at *L/c* reached almost zero. Theoretically, the transferred energy at the rod tip should be zero at *L/c* because the end was free. It was concluded that when analyzing the dynamic response of drill rods, the low-pass filtering should be adjusted to suit the resonant frequency of the drill rod system.

4. Conclusions

This study employed freely hung drill rods commonly used for in-situ tests, and the free end could be freely vibrated for estimating the natural dynamic response of the

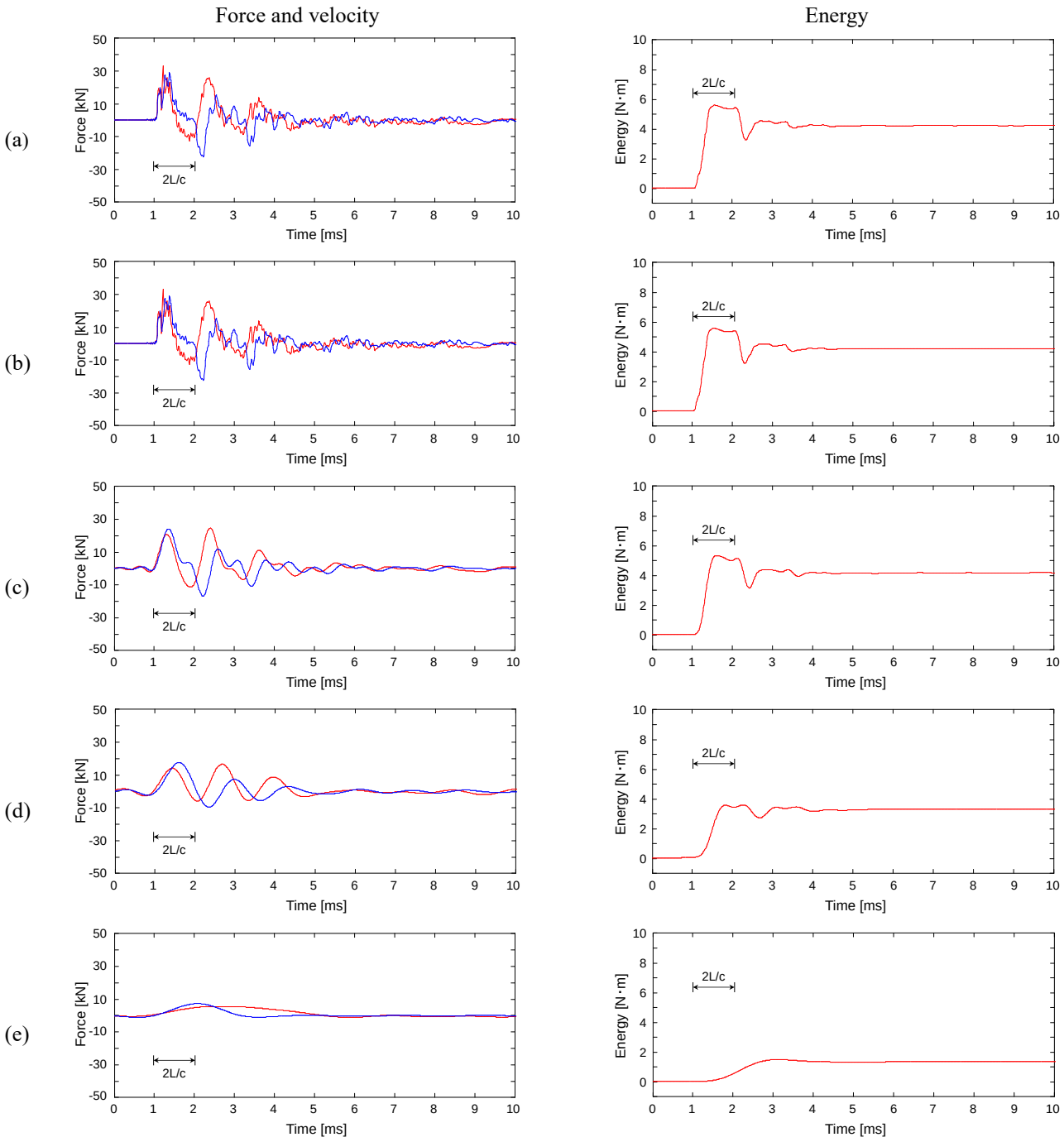

Fig. 10 Waveform variation for head with the rod length of 2 m according to low-pass filtering with cutoff frequencies of (a) 20 kHz, (b) 10 kHz, (c) 2 kHz, (d) 1 kHz, and (e) 0.5 kHz. Blue and red lines indicate the force and velocity signals, respectively

rod. The AW-type drill rods adopted in this study are conventionally used in SPT. The drill rods with three different total lengths were extended by couplers, and a 0.45-m-long instrumented rod installed with strain gauges and an accelerometer was connected at the rod head and tip. The dynamic responses and transferred energies were acquired under each impact by a pendulum hammer at the rod head. The notable findings are summarized below.

- At the heads of the drill rods, the force and velocity waveforms increased in proportion and the duration of *2L/c* increased with increasing length of the drill rod. The transferred energy peaked within the time *2L/c*, and the maximum energy increased with rod length owing to the longer *L* in *2L/c*. Conversely, at the rod tip, the first peak in the velocity waveform exceeded that determined from the force waveform owing to the large and tensile stress wave reflected at the tip. The

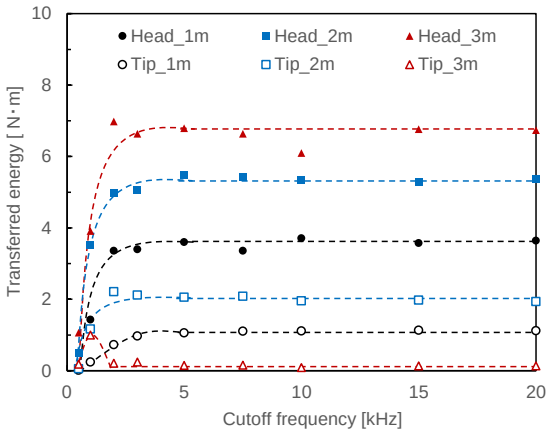

Fig. 11 Transferred energies along the cutoff frequency of low-pass filtering

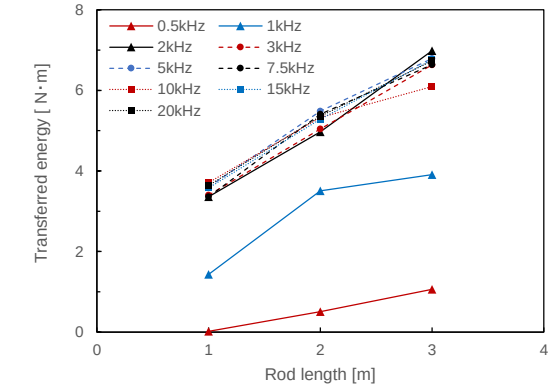

(a)

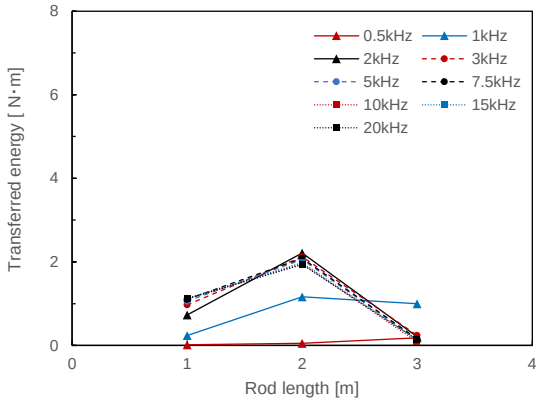

(b)

Fig. 12 Transferred energies along the length of drill rods at (a) head and (b) tip

transferred energy at the rod tip resembled a haversine pulse waveform that peaked within *L/c* and finally converged to zero.

- The resonant frequencies from the strain gauges decreased from 1.2 to 0.44 kHz as the rod length increased, and were similar at the rod head and tip. In contrast, the resonant frequencies from the accelerometer varied from 0.51 to 10.0 kHz, showing no trend with rod length. In addition, the resonant frequencies from the strain gauges were linearly related to their estimated natural frequencies with a high coefficient of determination. Thus, the dynamic responses from the strain gauges can more reliably capture the true responses than the accelerometer responses.
- After applying different cutoff frequencies (0.5–20 kHz), the force and velocity waveforms were perturbed at cutoff frequencies lower than 2 kHz. With these cutoff frequencies, the transferred energy varied regardless of rod length and instrumented location. At higher cutoff frequencies, the transferred energy at the rod head increased with rod length. At the tip of the 3-m-long rod, the transferred energy was almost zero, as theoretically expected under free-end boundary conditions. Therefore, the cutoff frequency in low-pass filtering should be adjusted in accordance with the resonant frequency.

Acknowledgments

This work was supported by the National Research Foundation of Korea (NRF) grant funded by the Korea government (MSIT) (No. NRF-2021R1A5A1032433).

References

Abou-matar, H. and Goble, G.G. (2004), "SPT dynamic analysis and measurements", In Current Practices and Future Trends in Deep Foundations, 441-462.

ASTM D1586 (2011), Test Method for Standard Penetration Test (SPT) and Split-Barrel Sampling of Soils; ASTM International: West Conshohocken, PA, USA. https://doi.org/10.1520/d1586-11

ASTM D4633 (2011), Standard Test Method for Energy Measurement for Dynamic Penetrometers, ASTM International, West Conshohocken, PA, USA.

ASTM D6951 (2011), Standard Test Method for Use of the Dynamic Cone Penetrometer in Shallow Pavement Applications, ASTM International, West Conshohocken, PA, USA.

Bajaj, K. and Anbazhagan, P. (2019), "Seismic site classification and correlation between VS and SPT-N for deep soil sites in Indo-Gangetic Basin", *Appl. Geophys.*, **163**, 55-72. https://doi.org/10.1016/j.jappgeo.2019.02.011.

Byun, Y.H. and Lee, J.S. (2013), "Instrumented dynamic cone penetrometer corrected with transferred energy into a cone tip: a laboratory study", *Geotech. Test. J.*, **36**(4), 533-542. https://doi.org/10.1520/gtj20120115.

Byun, Y.H., Yoon, H.K., Kim, Y.S., Hong, S.S. and Lee, J.S. (2014), "Active layer characterization by instrumented dynamic cone penetrometer in Ny-Alesund, Svalbard", *Cold Reg. Sci. Technol.*, **104**, 45-53. https://doi.org/10.1016/j.coldregions.2014.04.003.

Daniel, C.R., Howie, J.A., Jackson, R.S. and Walker, B. (2005), "Review of standard penetration test short rod corrections", *J. Geotech. Geoenviron. Eng.*, **131**(4), 489-497. https://doi.org/10.1061/(asce)1090-0241(2005)131:4(489).

Du, Y.J., Jiang, N.J., Liu, S.Y., Horpibulsuk, S. and Arulrajah, A. (2016), "Field evaluation of soft highway subgrade soil stabilized with calcium carbide residue", *Soils Found.*, **56**, 301-314.

Gabr, M.A., Hopkins, K., Coonse, J. and Hearne, T. (2000), "DCP criteria for performance evaluation of pavement layers", *J. Perform. Constr. Fac.*, **14**(4), 141-148. https://doi.org/10.1061/(asce)0887-3828(2000)14:4(141)

Hong, W.T., Byun, Y.H., Kim, S.Y. and Lee, J.S. (2016), "Cone penetrometer incorporated with dynamic cone penetration method for investigation of track substructures", *Smart Struct. Syst.*, **18**(2), 197-216. https://doi.org/10.12989/sss.2016.18.2.197.

Howie, J.A., Daniel, C.R., Jackson, R.S. and Walker, B. (2003), "Comparison of energy measurement methods in the standard penetration test", Report prepared for the US Bureau of Reclamation, Geotechnical Research Group, Department of Civil Engineering, The University of British Columbia, Vancouver, Canada.

Kim, S.Y., Hong, W.T. and Lee, J.S. (2019), "Role of the coefficient of uniformity on the California bearing ratio, penetration resistance, and small strain stiffness of coarse arctic soils", *Cold Reg. Sci. Technol.*, **160**, 230-241. https://doi.org/10.1016/j.coldregions.2019.02.012

Kim, S.Y. and Lee, J.S. (2020), "Energy correction of dynamic cone penetration index for reliable evaluation of shear strength in frozen sand–silt mixtures", *Acta Geotech.*, **15**(4), 947-961. https://doi.org/10.1007/s11440-019-00812-y.

Kleyn, E.G. (1975), "The Use of the Dynamic Cone Penetrometer (DCP)", Transvaal Roads Department, Report Number L2/74, Pretoria.

Kovacs, W.D. (1979), "Velocity measurement of free-fall SPT hammer", *J. Geotech. Geoenviron. Eng.*, **105**(1), 1-10. https://doi.org/10.1061/ajgeb6.0000748.

Kodicherla, S.P.K. and Nandyala, D.K. (2016), "Use of CPT and DCP based correlations in characterization of subgrade of a highway in Southern Ethiopia Region", *Int. J. Geo-Eng.*, **7**(1), 1-15. https://doi.org/ 10.1186/s40703-016-0025-8.

Langton, D.D. (1999), "The Panda lightweight penetrometer for soil investigation and monitoring material compaction", Ground Engineering.

Lee, C., Lee, J.S., An, S. and Lee, W. (2010), "Effect of secondary impacts on SPT rod energy and sampler penetration", *J. Geotech. Geoenviron. Eng.*, **136**(3), 522-526. https://doi.org/10.1061/(asce)gt.1943-5606.0000236.

Lee, J.S. and Byun, Y.H. (2020), "Instrumented cone penetrometer for dense layer characterization", *Sensors*, 20(20), 5782. https://doi.org/10.3390/s20205782.

Lee, J.S., Kim, S.Y., Hong, W.T. and Byun, Y.H. (2019), "Assessing subgrade strength using an instrumented dynamic cone penetrometer", *Soils Found.*, **59**(4), 930-941. https://doi.org/10.1016/j.sandf.2019.03.005.

Mir, M., Bouafia, A., Rahmani, K. and Aouali, N. (2017), "Analysis of load-settlement behaviour of shallow foundations in saturated clays based on CPT and DPT tests", *Geomech. Eng.*, **13**(1), 119-139. https://doi.org/10.12989/gae.2017.13.1.119.

Mohammadi, S.D., Nikoudel, M.R., Rahimi, H. and Khamehchiyan, M. (2008), "Application of the Dynamic Cone Penetrometer (DCP) for determination of the engineering parameters of sandy soils", *Eng. Geol.*, **101**(3-4), 195-203. https://doi.org/10.1016/j.enggeo.2008.05.006.

Morgano, C.M. and Liang, R. (1992), "Energy transfer in SPT-Rod length effect", In International conference on the application of stress-wave theory to piles, 121-127.

Odebrecht, E., Schnaid, F., Rocha, M.M. and de Paula Bernardes, G. (2005), "Energy efficiency for standard penetration tests", *J. Geotech. Geoenviron. Eng.*, **131**(10), 1252-1263. https://doi.org/10.1061/(asce)1090-0241(2005)131:10(1252).

Sancio, R.B. and Bray, J.D. (2005), "An assessment of the effect of rod length on SPT energy calculations based on measured field data", *Geotech. Test. J.*, **28**(1), 22-30. https://doi.org/10.1520/gtj11959.

Scala, A.J. (1956), "Simple methods of flexible pavement design using cone penetrometers", *New Zealand Eng.*, **11**(2), 34-44.

Seed, H.B., Tokimatsu, K., Harder, L.F. and Chung, R.M. (1985), "Influence of SPT procedures in soil liquefaction resistance evaluations", *J. Geotech. Eng.*, **111**(12), 1425-1445. https://doi.org/10.1061/(asce)0733-9410(1985)111:12(1425).

Skempton, A.W. (1986), "Standard penetration test procedures and the effects in sands of overburden pressure, relative density, particle size, ageing and overconsolidation", *Geotechnique*, **36**(3), 425-447. https://doi.org/10.1680/geot.1986.36.3.425.

Sujatha, E.R., Geetha, A.R., Jananee, R. and Karunya, S.R. (2018), "Strength and mechanical behaviour of coir reinforced lime stabilized soil", *Geomech. Eng.*, **16**(6), 627-634. https://doi.org/10.12989/gae.2018.16.6.627.

Webster, S.L., Grau, R.H. and Williams, T.P. (1992), "Description and Application of Dual Mass Dynamic Cone Penetrometer", Instruction Report GL-92-3, Department of the Army, US Army Corp of Engineers, Washington, DC.

Youd, T.L. and Idriss, I.M. (2001), "Liquefaction resistance of soils: summary report from the 1996 NCEER and 1998 NCEER/NSF workshops on evaluation of liquefaction resistance of soils", *J. Geotech. Geoenviron. Eng.*, **127**(4), 297-313. https://doi.org/10.1061/(asce)1090-0241(2001)127:4(297).

Sy, A. and Campanella, R.G. (1993), "Standard penetration test energy measurements using a system based upon the personal computer", *Can. Geotech. J.*, **30**, 876–882.

IC